Chemistry–A European Journal

Research Article
doi.org/10.1002/chem.202103853

Chemistry
Europe
European Chemical
Societies Publishing

www.chemeurj.org

Structural Insights into Hysteretic Spin-Crossover in a Set of Iron(II)-2,6-bis(1H-Pyrazol-1-yl)Pyridine) Complexes

Nithin Suryadevara[+],[a] Asato Mizuno[+],[a] Lea Spieker[+],[b] Soma Salamon,[b] Stephan Sleziona,[b] André Maas,[b] Erik Pollmann,[b] Benoît Heinrich,[c] Marika Schleberger,*[b] Heiko Wende,*[b] Senthil Kumar Kuppusamy,*[d] and Mario Ruben*[a, d, e]

Abstract: Bistable spin-crossover (SCO) complexes that undergo abrupt and hysteretic ($\Delta T_{1/2}$) spin-state switching are desirable for molecule-based switching and memory applications. In this study, we report on structural facets governing hysteretic SCO in a set of iron(II)-2,6-bis(1H-pyrazol-1-yl)pyridine) (bpp) complexes – [Fe(bpp–COOEt)$_2$](X)$_2$·CH$_3$NO$_2$ (X=ClO$_4$, **1**; X=BF$_4$, **2**). Stable spin-state switching – $T_{1/2}$ = 288 K; $\Delta T_{1/2}$ = 62 K – is observed for **1**, whereas **2** undergoes above-room-temperature lattice-solvent content-dependent SCO – $T_{1/2}$ = 331 K; $\Delta T_{1/2}$ = 43 K. Variable-temperature single-crystal X-ray diffraction studies of the complexes revealed pronounced molecular reorganizations – from the Jahn-Teller-distorted HS state to the less distorted LS state – and conformation switching of the ethyl group of the COOEt substituent upon SCO. Consequently, we propose that the large structural reorganizations rendered SCO hysteretic in **1** and **2**. Such insights shedding light on the molecular origin of thermal hysteresis might enable the design of technologically relevant molecule-based switching and memory elements.

[a] Dr. N. Suryadevara,[+] Dr. A. Mizuno,[+] Prof. Dr. M. Ruben
Institute of Nanotechnology (INT)
Karlsruhe Institute of Technology (KIT)
Hermann-von-Helmholtz-Platz 1
76344 Eggenstein-Leopoldshafen (Germany)
E-mail: mario.ruben@kit.edu

[b] L. Spieker,[+] Dr. S. Salamon, S. Sleziona, A. Maas, Dr. E. Pollmann,
Prof. Dr. M. Schleberger, Prof. Dr. H. Wende
University of Duisburg-Essen
Faculty of Physics and Center for Nanointegration Duisburg-Essen (CENIDE)
Lotharstraße 1, 47057 Duisburg (Germany)
E-mail: marika.schleberger@uni-due.de
        heiko.wende@uni-due.de

[c] Dr. B. Heinrich
Institut de Physique et Chimie des Matériaux de Strasbourg (IPCMS)
CNRS-Université de Strasbourg
23, rue du Loess, BP 43, 67034 Strasbourg Cedex 2 (France)

[d] Dr. S. K. Kuppusamy, Prof. Dr. M. Ruben
Institute for Quantum Materials and Technologies (IQMT)
Karlsruhe Institute of Technology (KIT)
Hermann-von-Helmholtz-Platz 1
76344 Eggenstein-Leopoldshafen (Germany)
E-mail: senthil.kuppusamy2@kit.edu

[e] Prof. Dr. M. Ruben
Centre Européen de Sciences Quantiques (CESQ)
Institut de Science et d'Ingénierie Supramoléculaires (ISIS)
8 allée Gaspard Monge, BP 70028, 67083 Strasbourg Cedex (France)

[+] These authors contributed equally to this manuscript.

📖 Supporting information for this article is available on the WWW under https://doi.org/10.1002/chem.202103853

Introduction

Bistable molecular magnetic materials showing magnetic or thermal hysteresis are proposed candidates for developing molecule-based switching and memory elements.[1] Single-molecule magnets (SMMs)[2] and spin-crossover (SCO)[3] complexes are two prominent classes of magnetic materials that show hysteresis. In an SMM, the hysteresis observed in the magnetization (M) versus field (H) plot is due to the presence of magnetic anisotropy and the associated spin-reversal barrier.[4] On the other hand, an SCO complex shows thermal hysteresis (ΔT) in the χT versus T plot, where χ and T stand for magnetic susceptibility and temperature, respectively. Crucially, SCO complexes show hysteretic spin-state switching (low-spin (LS)-to-high-spin (HS), and vice versa) well above the liquid nitrogen temperature, rendering them suitable for technological applications.[3a,5] While many examples of SCO complexes showing hysteretic spin-state switching have been reported,[1e,6] a clear elucidation of factors causing hysteretic switching in such complexes remains challenging.[7] Therefore, it is necessary to embark on systematic studies to obtain insights into factors contributing to the formation of thermal hysteresis in SCO complexes.

Iron(II)–bpp (bpp: 2,6-bis(1H-pyrazol-1-yl)pyridine) complexes are suitable systems for studying structural aspects governing hysteretic spin-state switching.[8] Because molecular organization in the crystal lattice of such complexes can be controlled by introducing functional groups at the pyridine and pyrazole fragments of the bpp skeleton, enabling the elucidation of structure – SCO property relationships.[9] For example, terpyridine-embrace-like packing of iron(II)–bpp cationic units in the crystal lattice has been attributed as a reason behind the hysteretic SCO observed in some iron(II)–bpp complexes.[10] In

Chem. Eur. J. 2022, 28, e202103853 (1 of 12)

© 2021 The Authors. Chemistry - A European Journal published by Wiley-VCH GmbH

Chemistry–A European Journal

Research Article
doi.org/10.1002/chem.202103853

**Chemistry
Europe**
European Chemical
Societies Publishing

another example, a rule based on the angular parameter ϕ (ϕ is the *trans*-$N_{pyrazole}$—Fe—$N_{pyrazole}$ angle) is proposed.[8a,11] The rule says that iron(II)–bpp complexes featuring $\phi \leq 172°$ are prone to be stabilized in the HS state, and the HS-to-LS switching is blocked due to the large structural reorganization required for the distorted HS state to attain a less distorted LS state. However, notable exceptions to the rule have been reported; that is, spin-state switching of some iron(II)–bpp complexes featuring $\phi \leq 172°$.[9b,11–12] Another notable example is [Fe-(bpp–COOEt)$_2$][ClO$_4$]$_2$·CH$_3$CN (bpp–COOEt stands for ethyl 2,6-bis(1*H*-pyrazol-1-yl)isonicotinate); the complex underwent spin-state switching ($T_{1/2} = 233$ K; $\Delta T_{1/2} = 100$ K (cycle 1)), despite featuring $\phi = 158.83°$.[12b] On the other hand, a similar complex – [Fe(bpp–COOC$_2$H$_5$)$_2$][ClO$_4$]$_2$·CH$_3$COCH$_3$ – reported by Coronado and co-workers underwent a LS-to-HS switching with $T_{1/2}$ centered around 330 K. Heating resulted in the loss of lattice acetone solvent, and the complex was trapped in the HS state; that is, in the subsequent cooling, HS-to-LS switching was not observed.[13] The foregoing discussion elucidates that HS-[Fe-(bpp–COOC$_2$H$_5$)$_2$][ClO$_4$]$_2$·solvent motif is prone to Jahn-Teller distortion, and the SCO is lattice solvent dependent. Spin-state switching in iron(II)–bpp complexes is also anion-dependent; that is, marked differences in the switching temperature and thermal hysteresis widths have been observed. Remarkably, to the best of our knowledge, SCO properties of [Fe-(bpp–COOC$_2$H$_5$)$_2$][BF$_4$]$_2$·solvent series of complexes are yet to be reported. These facets prompted us to prepare a set of nitromethane (CH$_3$NO$_2$) solvates of [Fe(bpp–COOC$_2$H$_5$)$_2$]$^{2+}$ system – [Fe(bpp–COOEt)$_2$](X)$_2$·CH$_3$NO$_2$ (X = ClO$_4$, **1**; X = BF$_4$, **2**; Figure 1) to elucidate structure – SCO property relationships. In the following sections, we discuss the single-crystal X-ray structures and spin-state switching characteristics of the complexes. Moreover, the molecular origin of thermal hysteresis observed in **1** and **2** is attributed to geometrical reorganization and ethyl group conformational switching that accompany spin-state switching.
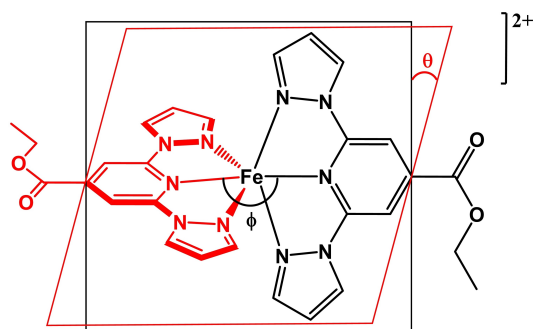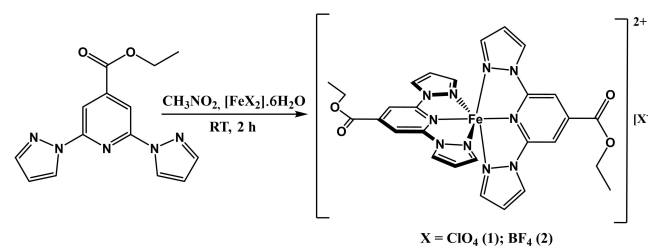
Results and Discussion

Preparation and thermogravimetric analyses of complexes 1 and 2

Complexes **1** and **2** were prepared by stirring bpp–COOEt ligand with the corresponding iron(II) salt in nitromethane for 2 h at room temperature, as depicted in Scheme 1. Slow diffusion of diethyl ether into the mother liquor at RT yielded predominantly wine-red crystals (**1-WR**) along with a few orange-colored crystals (**1-O**). In the case of **2**, only wine-red crystals (**2-WR**) were obtained. Elemental analyses of **1-WR**, **1-O**, and **2-WR** revealed the crystallization of the complexes with a lattice nitromethane solvent, as discussed in the next section.

To obtain insights into the thermal stability and lattice solvent desorption temperatures of the wine-red crystals of **1** and **2**, thermogravimetric analyses (TGA) were performed (Figure S1 in the Supporting Information) under ambient condition at a heating rate of 5 K min^{-1}. For **1-WR**, the onset of gradual weight loss started from 315 K and continued until 370 K. After that, the weight loss accelerated, and around 450 K a weight loss of 7.2% was obtained, indicating the complete loss of nitromethane solvent from the lattice (calcd: 6.92%). Above 480 K, degradation of the complex started. For complex **2-WR**, the solvent is not released below 350 K. The solvent release essentially occurs through a stepwise weight drop from 387 to 413 K; that is, 15 to 40 K above the boiling point (373 K) of nitromethane. The 7.5% weight drop agrees with the loss of one co-crystallized nitromethane molecule (calcd: 7.12%). Weight loss from degradation becomes significant above 500 K.

Keeping the crystals at room temperature resulted in the slow disintegration or cracking of them over time. Single-crystal X-ray diffraction and magnetometry studies were performed immediately after sample preparation. TGA, differential scanning calorimetry (DSC), Mössbauer, and Raman spectroscopic studies were performed a month after sample preparation. From the TGA analyses, it can be inferred that the samples retain lattice solvent molecules over time. Sample disintegration resulted in the modulation of SCO properties as inferred from the DSC and Mössbauer spectroscopic studies discussed below.

Figure 1. Molecular structures of [Fe(bpp–R)$_2$][X]$_2$·CH$_3$NO$_2$ (R = COOEt; X = ClO$_4$: **1**, BF$_4$: **2**) complexes discussed in this study. Counter anions and lattice solvent molecules are omitted for clarity. Phi (ϕ) is the *trans*-N(pyridyl)–Fe–N(pyridyl) angle; theta (θ) is the angle between the planes of two bpp ligands. Some HS iron(II)–bpp complexes featuring pronounced angular distortion in ϕ and θ undergo hysteretic spin-state switching, as observed for complexes **1** (HS; $\phi = 158.45°$) and **2** (HS; $\phi = 159.5°$).

Scheme 1. Preparation of complexes **1** and **2** discussed in this study.

Chemistry–A European Journal

Research Article
doi.org/10.1002/chem.202103853

Chemistry
Europe
European Chemical
Societies Publishing

Single-crystal X-ray structures of the complexes

Single-crystal X-ray diffraction (SCXRD) studies of **1-WR**, **1-O**, and **2-WR** revealed the crystallization of the complexes in the monoclinic $P2_1/n$ space group with one lattice nitromethane solvent per complex unit (Figures 2, and S2, Table 1). The asymmetric units contain one $[Fe(bpp\text{–}COOEt)_2](X)_2 \cdot CH_3NO_2$ unit (Figures S3 and S4), and the unit cells of the crystal lattices are composed of four complex units. The anions and the peripheral ethyl groups are disordered in the crystal lattices of the complexes. Average iron–nitrogen bond lengths and angular parameters collected in Table 1 indicate the LS and HS
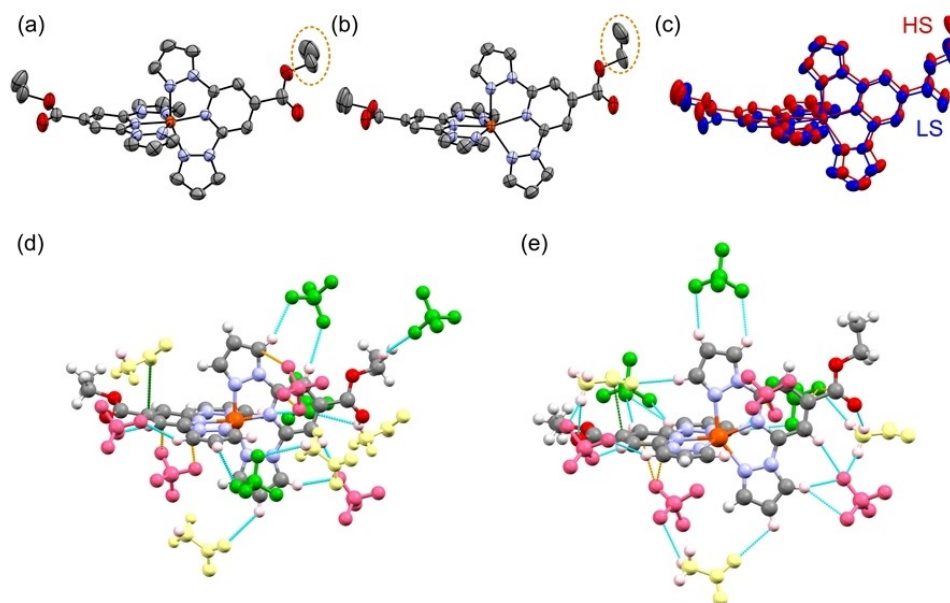

Figure 2. X-ray crystal structures of **1-WR** (LS) and **1-O** (HS) at 300 K. ORTEP diagrams of a) **1-WR** and b) **1-O** with the ellipsoids drawn at the 50% probability level. The orange dotted circles around the ethyl groups indicate the conformational switching of the group upon spin-state switching. c) Overlay of the LS (**1-WR**) and HS (**1-O**) forms of **1**, indicating the pronounced structural reorganization upon LS-to-HS switching. Intermolecular short contacts around d) **1-WR** and e) **1-O**. The intermolecular interactions are depicted in light blue (C–H···O interactions), orange (anion···π interactions), and green (O···C contacts) dotted lines. The most abundant parts of the disordered moieties are shown; other disordered parts are omitted for clarity. Equivalent ClO_4^- ions and CH_3NO_2 molecules are depicted in the same colors. The hydrogen atoms contributing to the hydrogen bonding interactions are depicted in light pink.

Table 1. Crystallographic data, bond lengths, and angular parameters of LS and HS forms of complex **1** at 300 K and LS and HS forms of complex **2** at 150 and 360 K, respectively.

	1-WR (300 K; LS)	**1-O** (300 K; HS)	**2-WR** (150 K; LS)	**2-O** (360 K; HS)
Formula	$C_{29}H_{29}Cl_2FeN_{11}O_{14}$	$C_{29}H_{29}Cl_2FeN_{11}O_{14}$	$C_{29}H_{29}B_2F_8FeN_{11}O_6$	$C_{29}H_{29}B_2F_8FeN_{11}O_6$
FW [g mol^{-1}]	882.38	882.46	857.10	857.10
Temperature [K]	300	300	150	360
Crystal dimensions [mm^3]	0.32×0.16×0.16	0.35×0.20×0.13	0.33×0.13×0.10	0.34×0.26×0.20
System	monoclinic	monoclinic	monoclinic	monoclinic
Space group	$P2_1/n$ (#14)	$P2_1/n$ (#14)	$P2_1/n$ (#14)	$P2_1/n$ (#14)
a [Å]	10.7048(2)	9.7181(2)	10.63453(6)	9.8874(8)
b [Å]	24.2312(4)	25.7973(4)	23.6122(4)	25.4314(16)
c [Å]	14.7020(3)	15.1984(2)	14.5050(2)	15.1739(9)
β [°]	98.509(2)	95.980(2)	99.2978(14)	96.512(7)
V [Å^3]	3771.58(12)	3789.52(11)	3594.42(10)	3790.9(5)
Z	4	4	4	4
Fe$_1$–N$_1$ (pyrazolyl)	1.974(2)	2.187(2)	1.9619(19)	2.191(8)
Fe$_1$–N$_3$ (pyridyl)	1.905(2)	2.1388(18)	1.8929(18)	2.128(7)
Fe$_1$–N$_5$ (pyrazolyl)	1.980(2)	2.156(2)	1.9736(19)	2.163(9)
Fe$_1$–N$_6$ (pyrazolyl)	1.985(3)	2.164(2)	1.9732(19)	2.154(9)
Fe$_1$–N$_8$ (pyridyl)	1.909(2)	2.1333(18)	1.8879(18)	2.144(7)
Fe$_1$–N$_{10}$ (pyrazolyl)	1.963(3)	2.184(2)	1.9540(19)	2.187(9)
rFe–N (average)	1.953	2.160	1.941	2.161
N$_3$–Fe$_1$–N$_8$ (ϕ)	171.25(10)	158.45(8)	172.50(8)	159.5(3)
θ	87.14(3)	80.50(2)	87.88(2)	81.79(9)
N$_6$–Fe$_1$–N$_{10}$ (ψ)	159.41(10)	145.74(8)	160.60(8)	144.9(3)
N$_1$–Fe$_1$–N$_5$ (ψ)	159.76(10)	145.47(8)	160.67(8)	145.6(3)
Σ	88.50	156.80	83.63	158.57

Chemistry–A European Journal

Research Article
doi.org/10.1002/chem.202103853

Chemistry Europe
European Chemical
Societies Publishing

states of **1-WR** and **1-O** at 300 K, respectively, and LS state of **2-WR** at 150 K.

To get insights into the structure of the LS and HS forms of **1** and **2**, variable temperature single-crystal X-ray diffraction studies were performed. For **1-WR**, such studies were performed at 150, 300, and 335 K. Angular parameters and bond lengths revealed the LS state of **1-WR** at 150 and 300 K (Table S2) and the isostructural nature of the structures obtained at 150 and 300 K (Figure S5). Further heating of **1-WR** crystal from 300 K to 335 K resulted in a color change from wine-red to orange, indicating the occurrence of in situ LS-to-HS switching. Structure determination of the in situ generated orange crystal at 335 K confirmed the HS state of it (Table S2), as well as the presence of lattice nitromethane solvent. Note, only 0.5% weight loss was observed for **1-WR** in the TGA analysis at 335 K, indicating that the crystal lattice can still hold the solvent at 335 K.

X-ray structures of **1-O** measured at 300 and 335 K revealed the HS state of the structures, as inferred from the bond lengths and angles collected in Tables 1 and S2. The variable temperature measurements also revealed the presence of lattice nitromethane solvent at 300 and 335 K. The structures of **1-O** obtained at 300 and 335 K are isostructural (Figure S6).

The structure of HS generated in situ from **1-WR** at 335 K and the structure of **1-O** determined at 300 K are isostructural (Tables S1 and S2, Figure S7). Due to the isostructural nature of the HS structures of **1-WR** (335 K) and **1-O** (300 K) generated in situ, the structure of **1-O** measured at 300 K is chosen as the HS reference for further discussion. On the other hand, the structure of **1-WR** measured at 300 K is chosen as a LS reference due to the isostructural nature of **1-WR** structures measured at 150 and 300 K (Figure S3). Moreover, choosing the HS and LS structures determined at the same temperature (300 K) aids meaningful comparisons between the HS and LS states of the complex, excluding temperature-induced effects, for example, lattice expansion.

The X-ray structure of **2-WR** determined at 150 K revealed its LS state at that temperature, as inferred from the bond lengths and angular parameters collected in Table 1. The structures of **1-WR** and **2-WR** determined at 150 K are isostructural (Figure S8). Heating **2-WR** to 360 K at 1 K min^{-1} resulted in the in situ switching of the complex to the HS state, hereafter denoted **2-O**. Structure determination at 360 K revealed the Jahn-Teller distorted nature of the HS state of **2**, as inferred from the angular parameters collected in Table 1. The structures of **1-O** and **2-O** determined at 335 and 360 K, respectively, are isostructural (Figure S9).

Figures 2d and e show the intermolecular short contacts around **1-WR** (LS) and **1-O** (HS). All the components – complex cation, anion, and lattice solvent – contribute to the C—H···O hydrogen bonding interactions around the iron complexes, as summarized in Tables S5 and S6. The structures are also characterized by anion···π interactions between the ClO_4^- ions and the BPP moieties (2.96–3.21 Å (HS), 3.13–3.16 Å (LS)), O···C contacts between the CH_3NO_2 molecules and the bpp moieties (3.18 Å (HS), 3.21 Å (LS)), and C···C contacts between the ester moieties and the bpp moieties (3.33–3.36 Å (HS), 3.40 Å (LS)). A

non-terpyridine-embrace lattice packing pattern (Figure S10) dictated by the intermolecular interactions, especially with the C—H···O hydrogen bonding interactions, was observed in the lattice. The overall structures are regarded as 3D hydrogen bond networks in both states of complex **1** (Figure S11).

Molecular organization in the crystal lattices of HS and LS forms of **2** followed a non-terpyridine-embrace lattice packing pattern (Figure S12). The intermolecular short contacts observed around **2-WR/LS** and **2-O/HS** are predominantly composed of C—H···O and C—H···F hydrogen bonding interactions (Figure S13, Tables S7 and S8). Overall, the packing and intermolecular interactions in the lattices of HS and LS forms of **2** are comparable with the molecular organization observed in the lattices of HS and LS forms of **1**.

Spin-state switching characteristics of complexes 1-WR and 2-WR

Magnetic measurements of **1-WR** and **2-WR** were performed at an applied field of 0.1 T. Due to the LS character of the complexes, and to ensure accurate measurements, the samples were brought to 340 (**1-WR**) and 335 K (**2-WR**) in order to ensure sufficient signal for precise positioning within the detection coils. For **1-WR**, χT value of 3.5 cm^3 mol^{-1} K^{-1} was obtained at 340 K, indicating the HS state of the complex at that temperature (Figure 3a). Cooling the sample at a rate of 3 K min^{-1} resulted in a gradual HS-to-LS transition followed by an abrupt one, as shown in Figure 3a. The χT value of 0.05 cm^3 mol^{-1} K^{-1} at 200 K indicates the LS state of the complex at that temperature; $T_{1/2\downarrow} = 257$ K was obtained for the cooling branch. Heating of the LS complex resulted in the LS-to-HS switching with $T_{1/2\uparrow} = 319$ K. Overall, $\Delta T_{1/2} = 62$ K and $T_{1/2} = 288$ K were deduced from the first heat-cool cycle. Similar SCO parameters were obtained in the second cool-heat cycle, elucidating the reproducible nature of the spin-state switching. To check for the scan rate dependence of $\Delta T_{1/2}$, measurements were performed at a scan rate of 1 K min^{-1} in the third cycle. The χT versus T plot obtained in the third cooling – heating cycle is comparable with the χT versus T plots obtained at a scan rate of 3 K min^{-1}, indicating that spin-state switching process associated with **1-WR** is scan rate independent. The small differences observed in the χT and $\Delta T_{1/2}$ values between the cycles are attributed to the fatigue experienced by the sample upon repeated cycling. Separate magnetic measurements of **1-O** crystals were not performed due to the small quantity of available sample material.

A second set of magnetic measurements was performed to assess the reproducibility of SCO characteristics of **1** by preparing a new batch of the complex. For the second set of measurements, a sample containing both **1-WR** and **1-O** was used. The SCO parameters – χT, $T_{1/2}$, and $\Delta T_{1/2}$ – obtained from the second set of measurements (Figure S14, first heating – cooling cycle) are comparable with the parameters obtained from the first set of measurements shown in Figure 3a, elucidating the reproducible nature of the spin-state switching characteristics of complex **1-WR**.
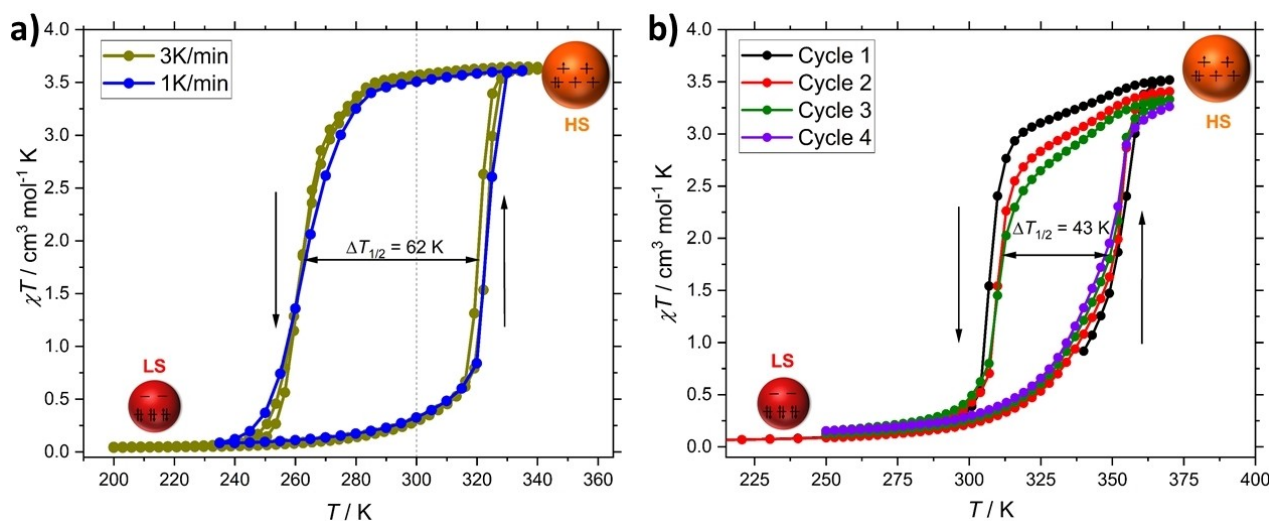
Figure 3. Spin-state switching characteristics of **1-WR** and **2-WR**. χT vs. T plots of a) **1-WR** and b) **2-WR**. The complexes showed temperature-induced bistable spin-state switching – $T_{1/2} = 288$ (**1-WR**) and 331 K (**2-WR**) – with remarkable thermal hysteresis widths: $\Delta T_{1/2} = 62$ (**1-WR**) and 43 K (**2-WR**). The dotted line at 300 K in (a) represents room temperature.

To get insights into the effect of lattice solvent desorption on the SCO properties of **1-WR**, experiments were performed in the 5 to 400 K temperature range (Figure S14, second and third cycles). A reduction in χT value was observed in the third cycle, tentatively attributed to the gradual loss of lattice nitromethane solvent and the concomitant disintegration of crystals.

Variable temperature measurements of complex **2-WR** at a scan rate of 3 K min^{-1} revealed its above RT SCO characteristic (Figure 3b). In the first LS-to-HS switching branch (Heat 1 in Figure 3b), $T_{1/2\uparrow} = 355$ K was obtained – a χT value of 3.45 cm^3 mol^{-1} K^{-1} at 370 K indicates the HS state of the complex at that temperature. In the subsequent cooling, the HS-to-LS transition was observed with $T_{1/2\downarrow} = 307$ K, and the LS state was reached around 280 K ($\chi T = 0.086$ cm^3 mol^{-1} K^{-1}). Overall, $\Delta T_{1/2} = 43$ K and $T_{1/2} = 331$ K were obtained for the first heat-cool cycle. In the subsequent cycles, a gradual decrease of χT values and hysteresis widths were observed due to the loss of lattice nitromethane solvent.

Although it is possible to perform magnetometry studies in the presence of solvent vapor to avoid lattice solvent desorption-mediated SCO alteration,[14] such studies are out of the scope of the present investigation. As the main focus of this study is the elucidation of structure-SCO property relation.

Differential scanning calorimetry (DSC) and Mössbauer spectroscopic studies

Differential scanning calorimetry (DSC) measurements were performed to substantiate the hysteretic nature of SCO of **1-WR** and **2-WR**. For **1-WR**, $T_{1/2\downarrow} = 269$ K, $T_{1/2\uparrow} = 319$ K, and $\Delta T_{1/2} = 50$ K were obtained in the first cycle (Figure S15 and Table S9). The trend observed in the magnetometry studies was reproduced (Table S9 and Table S10) in the subsequent cycles: Complex **2-WR** underwent a broad transition on heating, whose T_{MAX} (T_{MAX}

is the peak maximum) roughly coincides with $T_{1/2\uparrow}$ values obtained from magnetometry measurements (Figure S16 and Table S11). On cooling, two successive peaks were identified at 352 K and 312 K. The peak maxima values are comparable with the values – 353 and 309 K – obtained from the first derivative of χT versus T plot of the complex in the cooling branch of the second cycle (Figure S17); cycle two is taken as a representative example. The T_{MAX} values of the second transition obtained from the DSC studies are in close agreement with $T_{1/2\downarrow}$ obtained from magnetometry (Table S11). The enthalpy change of the second transition increases with the number of cycles while the onset temperature marginally shifts (Table S12). Such behavior is interpretable as the coexistence of two phases whose proportion is varying in successive cycles. This observation is in line with the χT versus T plots depicted in Figure 3b, where a change in spin-state composition was observed upon successive cycling. Overall, the trends observed in the DSC measurements serve as additional proof of hysteretic spin-state switching in **1-WR** and **2-WR**. The different values of $T_{1/2}$ and $\Delta T_{1/2}$ obtained from the magnetometry and DSC measurements are attributed to a possible temperature gradient felt by the samples during different measurements and cracking of the crystals over time, resulting in the alteration of SCO properties.

In addition to the magnetometry measurements, ^{57}Fe Mössbauer spectroscopy measurements were performed for complex **1-WR** at different temperatures to elucidate the spin-state composition of the sample. Such a study was not performed for complex **2-WR** due to the temperature limitation of 335 K associated with the instrument. Figure 4 shows the variable temperature Mössbauer spectra of **1-WR** at 300 and 335 K (heating); 300 and 200 K (cooling). The LS and HS contributions were fitted with an electric field gradient quadrupole distribution with linearly correlated chemical shifts. At 300 K, only one doublet from the LS state can be seen with an isomer shift $\delta_{LS} = 0.228$ mm s^{-1} (relative to α-Fe at room temper-

Chemistry–A European Journal

Research Article
doi.org/10.1002/chem.202103853

Chemistry Europe
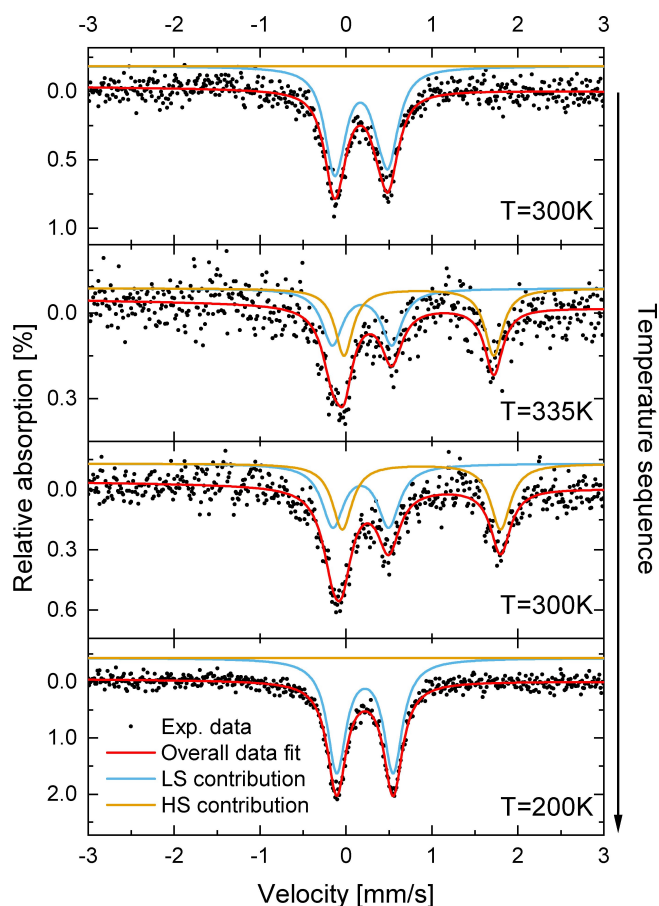European Chemical
Societies Publishing

Figure 4. ^{57}Fe Mössbauer studies of **1-WR** at 300, 335, and 200 K. The complex was heated from 300 to 335 K, leading to the observation of partial LS→HS switching: 51.7% HS state and 48.3% LS state. Cooling the sample from 335 to 300 K resulted in the retention of LS:HS mixture, thus indicating the hysteretic nature of the spin-state switching process. Subsequent cooling from 300 to 200 K led to the formation of pure LS state. To fit the data, an electric field gradient quadrupole distribution with linearly correlated chemical shifts was used, resulting in an isomer shift of $\delta_{LS} = 0.228$ (relative to α-Fe; 200 K) and 0.161 mm s^{-1}, $\delta_{HS} = 0.829$ mm s^{-1} (335 K). For the quadrupole splitting, the values $\Delta E_{Q(LS)} = 0.599$ mm s^{-1} (200 K) and $\Delta E_{Q(LS)} = 0.692$ mm s^{-1}, $\Delta E_{Q(HS)} = 1.745$ mm s^{-1} (335 K) were obtained.

ature) and a quadrupole splitting of $\Delta E_{Q(LS)} = 0.599$ mm s^{-1}. With increasing temperature, the LS doublet loses intensity in favour of an increase of the HS doublet. At 335 K, the HS state reaches its maximum value with a resonant area ratio of 51.7% over the LS state with 48.3%. Both doublets can be fitted with an isomer shift $\delta_{LS} = 0.161$ mm s^{-1}, $\delta_{HS} = 0.829$ mm s^{-1} and a quadrupole splitting of $\Delta E_{Q(LS)} = 0.692$ mm s^{-1}, $\Delta E_{Q(HS)} = 1.745$ mm s^{-1}. Similar to the magnetometry results, the continued presence of the HS state can be observed in the Mössbauer spectrum while cooling back to 300 K. This results in a small change of the ratio to a more dominant LS state contribution with 50.4% compared to 49.6% for the HS state. Here, the fit parameters $\delta_{LS} = 0.173$ mm s^{-1}, $\delta_{HS} = 0.877$ mm s^{-1} and $\Delta E_{Q(LS)} = 0.651$ mm s^{-1}, $\Delta E_{Q(HS)} = 1.843$ mm s^{-1} were used. In analogy to the magnetometry measurements, the Mössbauer spectrum at 200 K also shows the reversibility of the spin state to a pure LS state with

an isomer shift $\delta_{LS} = 0.221$ mm s^{-1}, and a quadrupole splitting of $\Delta E_{Q(LS)} = 0.657$ mm s^{-1}.

Unlike the 100% HS state obtained from the magnetometry measurements, only a 51.7% HS state was observed in the ^{57}Fe Mössbauer spectroscopic studies at 335 K. This discrepancy could have arisen due to different temperatures felt by the sample during the magnetometry and Mössbauer measurements. This assumption is meaningful considering the abrupt nature of the spin-state switching process associated with complex **1-WR** in the 330 to 340 K temperature range. It is also possible that the heater geometry necessary for Mössbauer spectroscopy could lead to a miniscule temperature gradient within the sample powder, causing a very small fraction to remain in the LS state. Another possibility for this discrepancy is the partial loss of lattice solvent due to long time required for the Mössbauer studies, with the sample held at elevated temperature for several hours. To conclude, the variable temperature ^{57}Fe Mössbauer spectroscopic study of **1-WR** reveals the LS state of the complex at 200 K and reversible nature of spin-state switching in good agreement with the hysteretic nature of χT versus T plots depicted in Figure 3a.

Small- and wide-angle X-ray scattering (SWAXS) and powder X-ray diffraction (PXRD) studies of complexes 1-WR and 2-WR

To check for the phase purity of the samples used for the measurements and for the analyses of temperature-dependent evolution of the crystalline phases, variable temperature SWAXS and PXRD studies of **1-WR** and **2-WR** were performed. Broad scattering peaks from average distances between molecular segments of an overall amorphous state were observed for **1-WR** (Figure S18a), revealing the loss of crystalline reflections. In general, SWAXS and PXRD require fine-crystalline powders, making it necessary to grind the sample to a coarse powder. Normally, grinding preserves the structure but the crystalline structure is lost upon grinding **1-WR**. This is obviously a consequence of the weak retention of solvent molecules by the lattice that was demonstrated by TGA; grinding heated up the sample and drove away the solvent from lattice positions, perturbing the regular arrangement of complex molecules. On the other hand, gently ground samples of **1-WR** revealed a crystalline phase comparable with the one generated from the SCXRD study at 300 K (Figure S18b). The crystallinity of **2-WR** is not affected by grinding. A comparison between the SCXRD and SWAXS patterns of **2-WR** (Figure S19) reveals that both structures are the same, with small changes of lattice parameters (Table S13) due to thermal expansion. The PXRD (**1-WR**) and SWAXS (**2-WR**) results indicate the phase purity of the samples used for the magnetometry, DSC, and ^{57}Fe Mössbauer spectroscopic studies.

The loss of crystallinity of **1-WR** upon grinding prohibited us from performing VT-SWAXS studies. For **2-WR**, such studies revealed a phase change on first heating in accordance with DSC, but the reverse transition is not observed on cooling (Figure S20). We attribute this to in situ solvent loss during
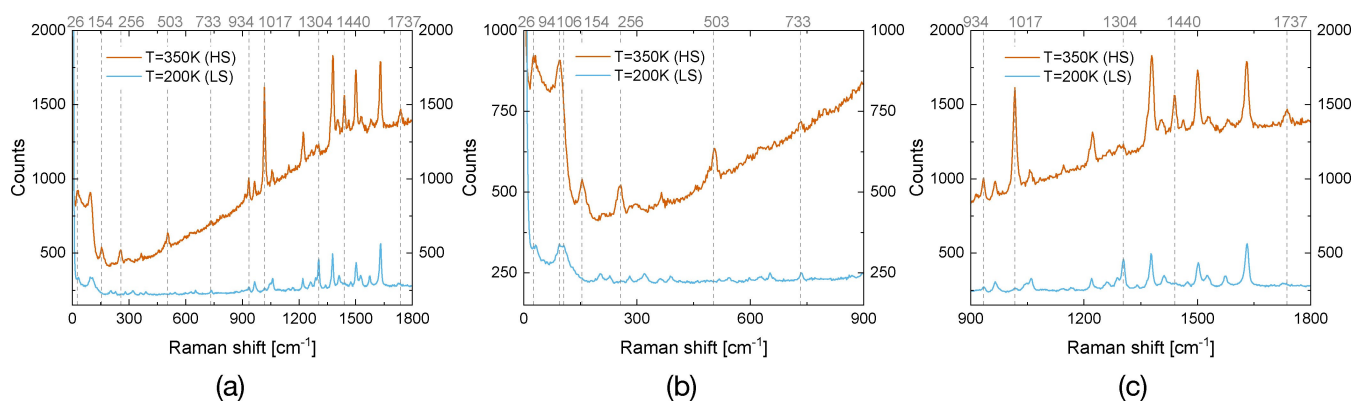
Chemistry–A European Journal

Research Article
doi.org/10.1002/chem.202103853

**Chemistry
Europe**
European Chemical
Societies Publishing

Figure 5. Raman spectra of **1-WR** at $T = 200$ (LS) and 350 K (HS). The most dominant changes are marked in gray. a) Overview of the whole spectra from 10 to 1800 cm^{-1}, plus enlargements of the regions b) from 10 to 900 cm^{-1} and c) from 900 to 1800 cm^{-1}.

SWAXS measurements, which required many hours (24–48 h) of data collection at each temperature.

Raman spectroscopic and optical microscopic studies

As inferred from the single-crystal X-ray studies, spin-state switching in **1-WR** and **2-WR** involves variations in iron(II)–nitrogen bond lengths and angles. Such variations can be observed by using Raman spectroscopy in a fast and nondestructive way, serving as proof of spin-state switching at a molecular level. Therefore, such studies could also be used as a diagnostic tool of spin-state switching, while studying the SCO properties of the complexes in the thin-film state. Consequently, we provide additional Raman spectroscopic proof of spin-state switching in **1-WR**; the complex is taken as a representative example.

Raman spectroscopic studies were performed from 1800 down to 10 cm^{-1} – at modes close to the Rayleigh Peak – at 200 and 300 K. An excitation wavelength (λ) of 532 nm and laser power (P_L) of 0.5 mW were used.

Pronounced changes were observed in the Raman spectra of **1-WR** upon heating the sample from 200 to 350 K, as indicated by the gray dashed lines in Figure 5. Low-frequency modes are of particular interest due to the elongation of the iron(II)–nitrogen bond lengths upon LS-to-HS switching, as shown by Lada et al., that Raman modes in the spectral region of 150 to 500 cm^{-1} are influenced by iron(II) centers.[15] It is due to the smaller vibrational energy of the iron(II)–nitrogen modes relative to the carbon–carbon, carbon–nitrogen, carbon–oxygen, and carbon–hydrogen modes. Upon LS-to-HS switching, new modes were observed at 154, 256, and 503 cm^{-1}, tentatively attributed to iron(II)–nitrogen bond length elongation (ca. 10%) upon spin-state switching.

We were also able to detect ultra-low-frequency modes below 150 cm^{-1} using the RayShield filter. The spectral region below 150 cm^{-1} is associated with vibrations arising from bonds composed of heavy atoms – in our case iron(II). Therefore, probing in the spectral region might lead to the observation of

frequency variations of iron(II)–nitrogen bonds upon spin-state switching. For **1-WR**, one vanishing mode at 106 cm^{-1}, one mode shifting from 94 to 97 cm^{-1}, and one significantly altering mode at 26–31 cm^{-1} were observed upon LS-to-HS switching, as shown in Figure 5b.

In addition to the low-frequency modes, changes in the high-frequency modes were also detected in the 900–1800 cm^{-1} range for **1-WR** upon LS-to-HS switching (Figure 5c). Significant changes in the intensities of vibrations centered around 934, 1017, 1304, 1440, and 1735 cm^{-1} were observed upon LS-to-HS switching. The most noticeable change was observed for the pyridine ring breathing mode at 1017 cm^{-1}.[16] The mode is coupled with the iron(II)–nitrogen bond length variation; therefore, the mode at 1017 cm^{-1} is used as a diagnostic mode to detect spin-state switching in iron(II)–bpp complexes.[17] The absence and presence of the pyridine ring breathing mode at 200 and 350 K, respectively, indicates temperature-induced LS-to-HS switching in **1-WR**, corroborating well with the magnetometry studies.

Optical microscopic studies were carried out to visually inspect the state of **1-WR** crystals upon spin-state switching. At 300 K, the crystal appeared dark gray/wine-red (Figure 6a) and the color changed to orange-red when heated to 350 K (Figure 6b). Upon subsequent cooling down to 300 K, the orange-red color was retained (Figure 6c), confirming the hysteretic behavior shown in Figure 3a. Further cooling to 200 K led to a change of color from orange-red to wine-red, indicating the thermochromic nature of the spin-state switching. Apart from the color change, pronounced changes in the crystal morphology were observed upon spin-state switching. Heating the **1-WR** crystal from 300 to 350 K resulted in its cracking. The crystal further cracked in the cooling cycle and pronounced differences between the morphologies of the original LS-crystal (300 K) and the LS-crystal obtained at 200 K after spin-state switching were observed. Such "self-grinding" – a term coined by Miyazaki et al.[18] – of molecular crystals upon spin-state switching was previously reported for iron(II) spin-crossover complexes.[12b,18]
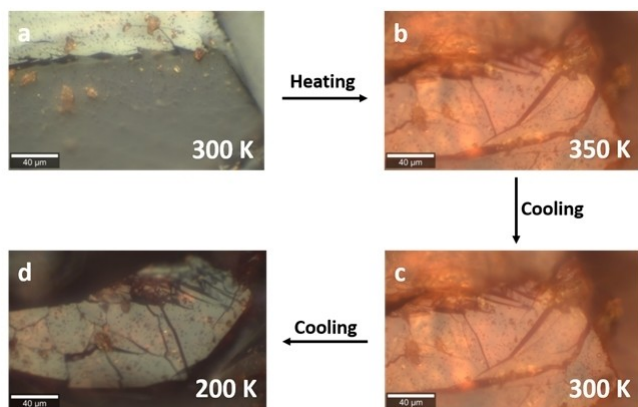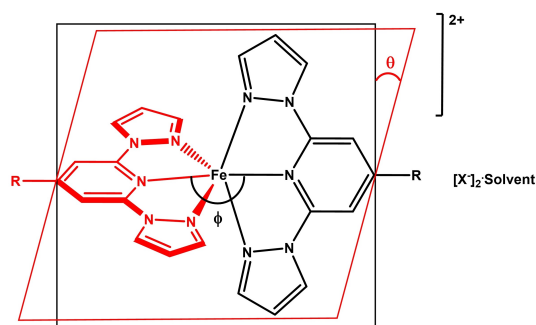
Chemistry–A European Journal

Research Article
doi.org/10.1002/chem.202103853

Chemistry
Europe
European Chemical
Societies Publishing

Figure 6. Optical microscopic studies of morphology changes in a **1-WR** crystal upon spin-state switching. a) LS form at 300 K, b) HS form at 350 K, c) HS form at 300 K, and d) LS form at 200 K. The different colors of LS and HS forms of 1-WR show the thermochromic nature of spin-state switching in the complex.

R = COOC$_2$H$_5$, X = ClO$_4^-$, Solvent = acetonitrile (3)
  COOH, X = BF$_4^-$ (4a) or ClO$_4^-$ (4b)
  CH=CH-Ph, X = BF$_4^-$, Solvent = acetone (5)
  NHCOCH$_3$, X = BF$_4^-$, Solvent = acetonitrile (6a) or
  X = ClO$_4^-$, Solvent = acetonitrile (6b)
  S-CH-(CH$_3$)$_2$, X = BF$_4^-$, Solvent = acetonitrile (7)
  SMe, X = BF$_4^-$ (8a) or ClO$_4^-$ (8b)
  C≡C, X = BF$_4^-$ (9)
  CH$_2$SCN, X = BF$_4^-$ (10)
  H, X = BF$_4^-$ (11)
  CH$_3$, X = ClO$_4^-$ (12)
  COOCH$_3$, X = ClO$_4^-$ (13)

Figure 7. Molecular structures of iron(II)–bpp complexes.

Discussion

Complexes **1-WR** and **2-WR** are two rare examples of the iron(II)–bpp family of complexes that show bistable spin-state switching characteristics with remarkable thermal hysteresis widths – 62 (**1-WR**, cycle 1) and 43 K (**2-WR**, cycle 1). The above RT spin-state switching of **2-WR** goes hand-in-hand with a gradual loss of lattice nitromethane solvent, rendering the SCO of the complex unstable to cycling. On the other hand, **1-WR** showed stable spin-state switching when cycled in the 5 to 340 K temperature range. Heat-cool cycling in the 5 to 400 K range led to lattice nitromethane solvent desorption and the SCO properties of **1-WR** were altered, as observed for **2-WR**. This observation is in line with the SCO properties of previously reported complex [Fe(bpp–COOEt)$_2$](ClO$_4$)$_2$·CH$_3$CN (**3**; Figure 5), whose spin-state switching characteristics varied upon repeated cycling.[12b] Heating complex **3** above RT resulted in the loss of lattice acetonitrile solvent and consequent stabilization of the LS state, as observed for the complexes discussed in this study. On a comparative scale, complexes **1-WR** and **2-WR** showed anion-dependent spin-state switching characteristics: complex **1-WR** containing ClO$_4^-$ switched at a lower temperature than its BF$_4^-$ counterpart, **2-WR**. The $T_{1/2}$ values of **1-WR** and **2-WR** follow the general trend observed for iron(II)–bpp complexes; that is, complexes containing ClO$_4^-$ anions switched at lower temperatures than the BF$_4^-$ containing complexes. Notable exceptions to this trend are complexes **4 a** ($T_{1/2} = 347$ K; BF$_4^-$)[13] and **4 b** (382 K; ClO$_4^-$)[19] shown in Figure 7.

While the role of anions and the presence or absence of lattice solvent in affecting the switching temperature and the nature of spin-state switching process – for example, gradual, abrupt, or bistable – is established, elucidation of factors contributing to the occurrence of thermal hysteresis in iron(II)–bpp family of complexes remains tentative. Such elucidation is not straightforward considering many parameters affecting the spin-state switching process. Nevertheless, we have attempted to propose structure – SCO property relationships for **1** and **2**. Such proposal is based on the experimental observations presented in the previous sections, inferences obtained from the observations, and comparing the inferences with previous insights reported in the literature.

The occurrence of SCO with narrow thermal hysteresis widths ($\Delta T_{1/2} = 1$ to 4 K) in some iron(II)–bpp complexes is attributed to a terpyridine-embrace-like packing pattern of molecules in the crystal lattice.[10] On the contrary, complexes **1-WR** and **2-WR** adopt non-terpyridine-embrace-like packing patterns in their lattices, indicating factors other than terpyridine-embrace-like molecular organization contributing to the occurrence of hysteretic SCO in the complexes.

One such factor is the molecular distortion that renders spin-state switching hysteretic in iron(II)–bpp complexes.[11–12,20] A select class of iron(II)–bpp complexes featuring pronounced Jahn-Teller distortion – represented by ϕ in Figures 1 and 7 – in their HS state have been reported to undergo hysteretic spin-state switching (Table 2). The angular parameters – ϕ and θ – of such complexes (Figure 7) and the difference between the angular parameters of LS and HS states of the complexes – $\Delta\phi$ and $\Delta\theta$ – are collected in Table 2. From the table, it can be inferred that low-spin iron(II)–bpp–R complexes show ϕ and θ values close to 180° and 90°, respectively. High-spin iron(II)–bpp complexes show a range of ϕ and θ values – $150° \leq \phi \leq 180°$ and $70° \leq \theta \leq 90°$.

In general, HS iron(II)–bpp–R systems featuring pronounced angular distortions in ϕ are trapped in the HS state, and it has been reasoned that complexes with $\phi \leq 172°$ are prone to be kinetically stabilized in the HS state.[8a] The reasoning is logical considering the large geometrical reorganization a distorted HS molecule should undergo to reach a relatively less distorted LS

Chemistry–A European Journal

Research Article
doi.org/10.1002/chem.202103853

Chemistry Europe
European Chemical
Societies Publishing

Table 2. Angular parameters and thermal hysteresis widths of iron(II)–bpp–R complexes depicted in Figure 7.

Complex	ϕ [°]		θ [°]		$\Delta\phi$ [°]	$\Delta\theta$ [°]	$\Delta T_{1/2}$ [K]
	LS	HS	LS	HS			
1	171.25(10)	158.45(8)	87.14(3)	80.50(2)	12.8	6.64	62
2	172.50(8)	159.5(3)	87.88(2)	81.79(9)	13.0	6.09	43
3	–	158.83(17)	–	78.74(10)	–	–	100
4a	180	180	87.6	88.8	0	−0.8	3
4b	180	180	88	89	0	−1	3
5	175.25(13)	161.92(10)	77.65	73	13.33 (16)	4.65	15
6a	174.4(2)	167.79(11)	87.35(6)	83.79(5)	6.6(2)	3.56(1)	12
6b	178.25(18)	173.15(10)	89.31	89.99	7.95(6)	2.9(2)	7
7	174.33(7)	167.8(2)	88.76(2)	86.89(6)	6.517	1.866	17
8a	175.2(2)	168.3(2)	87.76(4)	86.55(5)	7	1.2	2
8b	177.9(2)	168.89(19)	89.12(5)	87.14(4)	9.01	1.98	3
9	177.14	172.12	85.13	79.99	5.02	5.14	8
10	178.22(6)	172.34(8)	88.7	88.5	5.88	0.2	0
11	178.25(18)	173.15(10)	89.31	89.99	5.1	0.68	3
12	–	163.72	–	89.48	–	–	18
13	–	158.77(5)	–	80.738(12)			

state. Such geometrical reorganization should be accommodated in the crystal lattice – for example, tight packing of complex entities and high density of crystals blocks such reorganization,[20a] thereby HS-to-LS switching is blocked. However, some distorted iron(II)–bpp complexes (**1**, **2**, **3**,[12b] **5**,[20b] **6a**,[12a] **7**,[21] **8a**,[22] **8b**,[22] and **12**[11]) featuring $\phi \leq 172°$ undergo spin-state switching with pronounced $\Delta T_{1/2}$. Moreover, complexes **5**, **6a**, **6b**, and **7** all showing remarkable $\Delta T_{1/2}$ values underwent twisting of bpp ligands ($\Delta\theta$) upon spin-state switching. Based on the above discussion, it can be inferred that complexes that show pronounced rotation and twisting of ligands upon SCO are prone to exhibit hysteretic spin-state switching.

The variable-temperature SCXRD studies of **1** and **2** discussed above revealed the Jahn-Teller-distorted nature of their HS states and a close to ideal octahedral geometry of their LS states. The respective *trans*-N(pyridyl)–Fe–N(pyridyl) angles (ϕ) of LS (**1-WR**) and HS (**1-O**) complexes are 171.25(10)° and 158.45(8)°, indicating a large geometric modulation – $\Delta\phi = 12.8°$ – associated with the switching process. Moreover, LS-to-HS switching in **1** also involves twisting of ligands as inferred from the θ values – **1-WR** = 87.14(3)° and **1-O** = 80.50(2)°; $\Delta\theta = 6.64°$. Similar geometric modulations occurred in the lattice of **2** – $\Delta\phi = 13°$ and $\Delta\theta = 6.09°$ (Table 2). The observed values of $\Delta\phi$ and $\Delta\theta$ for **1** and **2** are among the highest values so far reported for iron(II)–bpp complexes (Table 2).

Several other iron(II)–bpp complexes with distorted HS state whose LS structures are not available – for example, complexes **3**[12b] and **12**[11] (Figure 7 and Table 2) – have also undergone hysteretic spin-state switching, pointing towards the origin of hysteretic spin-state switching in **1** and **2** to molecular distortion. Outliers to the above discussion relating to distortion and thermal hysteresis are complexes **4a**[13] and **4b**[19] and **10**. The HS structures of **4a** and **4b** are more planar than their LS counterparts, yet the complexes show $\Delta T_{1/2} = \sim3$ K. Complex **10**[23] underwent a non-hysteretic spin-state interconversion despite featuring $\Delta\phi = 5.5°$. However, $\Delta\theta = 0.2°$ indicates a negligible twisting of bpp ligands of **10** upon SCO. These facets indicate that pronounced twisting and rotation of bpp ligands

are required for a complex to undergo hysteretic spin-state switching, as observed in the cases of **1**, **2**, **5**, **6a**, **6b**, **7**, and **9**.[24]

Analyses of the X-ray structures of LS and HS states of complexes **1** and **2** reveal conformational switching of one of the ethyl groups upon spin-state switching (Figures 2 and S2). In the HS-state, the ethyl groups are organized in plane with the bpp skeleton, whereas an approximately 90° perpendicular flipping of the ethyl group relative to the plane of the pyrazolyl rings is observed in the LS structure. This observation is in line with the studies detailing anion[7b,25] or ligand substituent[26] conformation-mediated hysteretic spin-state switching. Therefore, it is reasonable to conclude that conformational switching of ethyl groups going hand-in-hand with shape variation, quantified by $\Delta\phi$ and $\Delta\theta$, effected the occurrence of hysteretic spin-state switching in **1** and **2**.

Intermolecular interactions between the lattice solvents, anions, and switching entities propagate the switching event throughout the lattice, rendering the switching process cooperative.[27] Apart from mediating the propagation of the spin-state switching throughout the lattice, solvent molecules present in the lattices of **1** and **2** provided the required free volume, thereby the large geometrical reorganizations upon SCO are well accommodated in the crystal lattices of the complexes.[20a] The trapping of the lattice solvent-free complex – [Fe(BPP–COOMe)₂][ClO₄]₂ (**13**); $\phi = 158°$ – in the HS state[28] is an indication that the presence of lattice solvent facilitates the occurrence of SCO in complexes **1** and **2**. Although the forgoing point is not a cause-and-effect relationship due to the non-isomorphous nature of **1** and **2** with **13**, it is in line with a recent report by Halcrow and co-workers elucidating that SCO is controlled by the number of lattice solvent molecules present in a crystal. Complexes **6a·**MeCN and **6b·**MeCN underwent HS-to-LS switching upon cooling. Whereas complexes **6a·**2MeCN and **6b·**2MeCN remained trapped in the HS state.[12a]

The foregoing discussion elucidates that complexes belong to [Fe(bpp–COOEt)₂]²⁺ family are a rare class of bistable SCO systems. The favorable conditions in the crystal lattice and pronounced shape change and substituent conformation

Chemistry–A European Journal

Research Article
doi.org/10.1002/chem.202103853

Chemistry Europe
European Chemical
Societies Publishing

switching rendered SCO of the complexes hysteretic. It would be interesting to study further by increasing the alkyl chain length in small increments – for example, by preparing complexes with C_3 and C_4 alkyl substituents. Such proposal is grounded on the non-hysteretic nature of spin-state switching observed in iron(II)–bpp–COOR complexes featuring long alkyl chains.[29]

Iron(II)–bpp complexes are also known to undergo LIESST (light-induced excited spin-state trapping) mediated LS-to-HS switching at low temperatures.[30] Such studies in the future might give additional insights into structure – SCO property relationships for complexes **1** and **2**, as recently reported for a family of iron(II)–BPP complexes.[31]

Conclusions

In summary, we have reported the bistable SCO characteristics of complexes **1-WR** ($\Delta T_{1/2} = 62$ K and $T_{1/2} = 288$ K) and **2-WR** ($\Delta T_{1/2} = 43$ K and $T_{1/2} = 331$ K). The distorted nature of their high-spin structures and the associated structural reorganization required to attain the less-distorted low-spin state and the conformational variation of the ethyl groups upon spin-state switching are attributed as the molecular origin of the hysteretic spin-state switching observed for the complexes. The hysteretic SCO profiles observed for the complexes in the vicinity of room temperature show that mononuclear SCO complexes with device-suitable switching characteristics could be obtained. Overall, the hysteretic nature of the SCO observed for complexes **1-WR** and **2-WR** and the structure – SCO property insights obtained from the VT-XRD, magnetometry, and Raman and optical microscopic studies are encouraging for studying iron(II)–bpp complexes for practical device applications.

Experimental Section

Anhydrous solvents and Fe(ClO$_4$)$_2$·6H$_2$O were purchased from commercial sources and used as received. All the reactions were performed under argon. Electrospray ionization mass spectrometry (ESI-MS) data were acquired with a Bruker micrOTOF-Q II spectrometer. Infrared spectra were recorded with a MAGNA FTIR, Nicolet spectrometer in the region of 4000–400 cm^{-1}. The samples for IR were prepared by grinding the compounds with dry KBr, and the mixture was made into pellets for measurements.

General procedure for the preparation of complexes 1 and 2: Ligand **L** (160 mg, 0.565 mmol, 2 equiv.) was suspended in dry nitromethane (10 mL). A solution of Fe(X)$_2$·6H$_2$O (0.282 mmol, 1 equiv.) in nitromethane (8 mL) was added drop-wise to the above solution, and a red solution was formed on addition. The resulting mixture was stirred under argon for 2 h. Solvents were evaporated under reduced pressure. The mixture was dissolved in a minimum amount of nitromethane, and diethyl ether (DEE) was slowly diffused to obtain a crystalline dark red color complex.

Complex 1: Yield: 80 mg (32.3%). ESI-MS, found (calcd): 721.1083 [$M-ClO_4$]$^+$, (721.0974). IR (KBr, cm^{-1}): 3116, 2984, 1729, 1630, 1572, 1546, 1524, 1499, 1459, 1405, 1377, 1338, 1287, 1252, 1137, 1085, 1049, 970, 911, 862, 791, 763, 621, 599. Elemental analysis for

FeC$_{28}$H$_{26}$N$_{10}$Cl$_2$O$_8$·CH$_3$NO$_2$, found (calcd): C 39.16 (39.48), H 3.03 (3.31), N 17.17 (17.46).

CAUTION! Perchlorate-containing complexes are potential explosives. Therefore, such complexes should be handled with care. Thermogravimetric analyses (TGA) could be performed to determine the decomposition temperatures of the complexes.

Complex 2: Yield: 62 mg (31%). ESI-MS, found (calcd): 709.1517 [$M-BF_4$]$^+$, (709.1600); 657.1243 [$M-2BF_4+Cl$]$^+$, (657.1172). IR (KBr, cm^{-1}): 3121, 2985, 1726, 1630, 1573, 1546, 1525, 1498, 1471, 1407, 1378, 1340, 1287, 1253, 1137, 1029, 970, 911, 792, 764, 654, 600, 521. Elemental analysis for FeC$_{28}$H$_{26}$N$_{10}$B$_2$F$_8$·CH$_3$NO$_2$, found (calcd): C 40.06 (40.64), H 3.36 (3.41), N 17.59 (17.98).

DSC and TGA measurements: DSC measurements were performed with a TA Instruments DSCQ 1000 instrument operated at a scan rate of 2 Kmin^{-1} on heating and on cooling. TGA measurements were performed with a TA Instruments Q50 instrument operated at a scanning rate of 5 Kmin^{-1}.

X-ray diffraction studies: Single-crystal X-ray diffraction data were collected using STOE IPDS2T diffractometer with graphite monochromated Mo$_{K\alpha}$ radiation ($\lambda = 0.71073$ Å). Crystals were mounted on a loop using oil or on a glass capillary, and the X-ray diffraction data were collected under a nitrogen stream. The frame data were integrated and corrected for absorption with CrysAlisPro.[32] The structures were solved using dual space methods (SHELXT 2018/2)[33] and were refined with full-matrix least-squares procedures on F^2 using SHELXL 2018/3[34] implemented in Olex2.[35] All non-hydrogen atoms were refined anisotropically, and all hydrogen atoms were placed at calculated positions and refined using a riding model. Disordered perchlorate anions and alkyl chains were refined with restrains (SADI, DFIX, SIMU, and RIGU commands) and constraints (EADP commands) on the bond lengths and the anisotropic displacement parameters. The occupancies of the disordered components are mentioned in the Supporting Information. The angular parameters discussed in the study are obtained using OctaDist.[36]

Deposition Numbers 2098682 (for **1-WR**/LS at 150 K), 2098683 (for **1-WR**/LS at 300 K), 2098684 (for **1-WR**/HS at 335 K), 2098685 (for **1-O**/HS at 300 K), 2098686 (for **1-O**/HS at 335 K), 2098687 (for **2-WR**/LS at 150 K) and 2098688 (for **2-O**/HS at 360 K) contain the supplementary crystallographic data for this paper. These data are provided free of charge by the joint Cambridge Crystallographic Data Centre and Fachinformationszentrum Karlsruhe Access Structures service.

Magnetometry: Magnetic properties were investigated with the vibrating sample magnetometer (VSM) option of a Quantum Design PPMS DynaCool. The temperature-dependent measurements were performed under an applied magnetic field of 0.1 T at temperature sweep rates of 3 and 1 Kmin^{-1}.

Mössbauer spectroscopy: ^{57}Fe Mössbauer spectra were recorded on powder samples in transmission geometry, using a ~50 mCi ^{57}Co radiation source mounted on a constant-acceleration Mössbauer driving unit (WissEl GmbH). Temperature control was achieved by means of a closed-cycle cryostat (Lakeshore) using a heated sample holder assembly.

Small- and wide-angle X-ray scattering (SWAXS) and powder X-ray diffraction (PXRD) studies: The SWAXS/PXRD patterns were obtained with a transmission Guinier-like geometry. A linear focalized monochromatic Cu Kα1 beam ($\lambda = 1.54056$ Å) was obtained using a sealed-tube generator (600 W) equipped with a bent quartz monochromator. The samples were filled in sealed cells of adjustable path. The sample temperature was controlled within ± 0.1 °C, and exposure times were varied from 4 to 24 h. The

Chemistry–A European Journal

Research Article
doi.org/10.1002/chem.202103853

Chemistry
Europe
European Chemical
Societies Publishing

patterns were recorded on image plates scanned by Amersham Typhoon IP with 25 µm resolution (periodicities up to 120 Å). I(2theta) profiles were obtained from images, by using home-developed software.

Raman spectroscopy and optical microscopy: Raman backscattering measurements were carried out with a WITec alpha300 RA in combination with a vacuum cooling stage from Linkam (THMS350EV). For all spectra, the laser wavelength was 532 nm with a laser power of 0.5 mW to avoid heating effects. The laser was focused using an objective Zeiss LD "Epiplan-Neofluar" 50x with a numerical aperture of 0.55, which was also used for the optical images. For the temperature-dependent measurements, the sample was in a nitrogen atmosphere and cooled with liquid nitrogen by using a Linkam vacuum cooling stage. To obtain ultralow frequency modes down to 10 cm^{-1}, a RayShield filter was used.

Acknowledgements

Conflict of Interest

The authors declare no conflict of interest.

Data Availability Statement

The data that support the findings of this study are openly available in CCDC at https://www.ccdc.cam.ac.uk/, reference number 2098682.

[1] a) W. Fujita, K. Awaga, *Science* **1999**, *286*, 261–262; b) R. G. Hicks, *Nat. Chem.* **2011**, *3*, 189–191; c) V. I. Minkin, *Russ. Chem. Bull.* **2008**, *57*, 687–717; d) I. Ratera, J. Veciana, *Chem. Soc. Rev.* **2012**, *41*, 303–349; e) Z.-S. Yao, Z. Tang, J. Tao, *Chem. Commun.* **2020**, *56*, 2071–2086.

[2] a) C. H. Chen, L. Spree, E. Koutsouflakis, D. S. Krylov, F. P. Liu, A. Brandenburg, G. Velkos, S. Schimmel, S. M. Avdoshenko, A. Fedorov, E. Weschke, F. Choueikani, P. Ohresser, J. Dreiser, B. Buchner, A. A. Popov, *Adv. Sci.* **2021**, *8*, 2000777; b) C. A. P. Goodwin, F. Ortu, D. Reta, N. F. Chilton, D. P. Mills, *Nature* **2017**, *548*, 439–442; c) N. Ishikawa, M. Sugita, T. Ishikawa, S. Koshihara, Y. Kaizu, *J. Am. Chem. Soc.* **2003**, *125*, 8694–8695; d) E. M. Pineda, T. Komeda, K. Katoh, M. Yamashita, M. Ruben, *Dalton Trans.* **2016**, *45*, 18417–18433; e) R. Sessoli, D. Gatteschi, A. Caneschi, M. A. Novak, *Nature* **1993**, *365*, 141–143.

[3] a) O. Kahn, *Curr. Opin. Solid State Mater. Sci.* **1996**, *1*, 547–554; b) K. S. Kumar, M. Ruben, *Coord. Chem. Rev.* **2017**, *346*, 176–205.

[4] D. Gatteschi, *J. Alloys Compd.* **2001**, *317–318*, 8–12.

[5] O. Kahn, C. J. Martinez, *Science* **1998**, *279*, 44–48.

[6] a) B. Weber, W. Bauer, J. Obel, *Angew. Chem. Int. Ed.* **2008**, *47*, 10098–10101; *Angew. Chem.* **2008**, *120*, 10252–10255; b) B. Weber, E. Kaps, J. Weigand, C. Carbonera, J.-F. Létard, K. Achterhold, F. G. Parak, *Inorg. Chem.* **2008**, *47*, 487–496; c) B. Schäfer, C. Rajnák, I. Šalitroš, O. Fuhr, D. Klar, C. Schmitz-Antoniak, E. Weschke, H. Wende, M. Ruben, *Chem. Commun.* **2013**, *49*, 10986–10988; d) M. A. Halcrow, *Chem. Lett.* **2014**, *43*, 1178–1188; e) C. Lochenie, W. Bauer, A. P. Railliet, S. Schlamp, Y. Garcia, B. Weber, *Inorg. Chem.* **2014**, *53*, 11563–11572; f) S. Zheng, N. R. M. Reintjens, M. A. Siegler, O. Roubeau, E. Bouwman, A. Rudavskyi, R. W. A. Havenith, S. Bonnet, *Chem. Eur. J.* **2016**, *22*, 331–339; g) H. Hagiwara, T. Masuda, T. Ohno, M. Suzuki, T. Udagawa, K.-i. Murai, *Cryst. Growth Des.* **2017**, *17*, 6006–6019; h) K. Ridier, G. Molnár, L. Salmon, W. Nicolazzi, A. Bousseksou, *Solid State Sci.* **2017**, *74*, A1–A22; i) K. Senthil Kumar, N. Del Giudice, B. Heinrich, L. Douce, M. Ruben, *Dalton Trans.* **2020**, *49*, 14258–14267; j) E. Tailleur, M. Marchivie, N. Daro, G. Chastanet, P. Guionneau, *Chem. Commun.* **2017**, *53*, 4763–4766.

[7] a) B. Weber, W. Bauer, T. Pfaffeneder, M. M. Dîrtu, A. D. Naik, A. Rotaru, Y. Garcia, *Eur. J. Inorg. Chem.* **2011**, *2011*, 3193–3206; b) N. Phukkaphan, D. L. Cruickshank, K. S. Murray, W. Phonsri, P. Harding, D. J. Harding, *Chem. Commun.* **2017**, *53*, 9801–9804.

[8] a) M. A. Halcrow, *Coord. Chem. Rev.* **2009**, *253*, 2493–2514; b) J. M. Holland, J. A. McAllister, Z. Lu, C. A. Kilner, M. Thornton-Pett, M. A. Halcrow, *Chem. Commun.* **2001**, 577–578; c) V. A. Money, I. Radosavljevic Evans, M. A. Halcrow, A. E. Goeta, J. A. K. Howard, *Chem. Commun.* **2003**, 158–159; d) M. A. Halcrow, *Coord. Chem. Rev.* **2005**, *249*, 2880–2908; e) M. A. Halcrow, *New J. Chem.* **2014**, *38*, 1868–1882; f) L. J. Kershaw Cook, R. Mohammed, G. Sherborne, T. D. Roberts, S. Alvarez, M. A. Halcrow, *Coord. Chem. Rev.* **2015**, *289–290*, 2–12; g) R. J. Deeth, M. A. Halcrow, L. J. Kershaw Cook, P. R. Raithby, *Chem. Eur. J.* **2018**, *24*, 5204–5212.

[9] a) L. J. Kershaw Cook, R. Kulmaczewski, R. Mohammed, S. Dudley, S. A. Barrett, M. A. Little, R. J. Deeth, M. A. Halcrow, *Angew. Chem. Int. Ed.* **2016**, *55*, 4327–4331; *Angew. Chem.* **2016**, *128*, 4399–4403; b) M. A. Halcrow, I. Capel Berdiell, C. M. Pask, R. Kulmaczewski, *Inorg. Chem.* **2019**, *58*, 9811–9821.

[10] R. Pritchard, C. A. Kilner, M. A. Halcrow, *Chem. Commun.* **2007**, 577–579.

[11] L. J. K. Cook, F. L. Thorp-Greenwood, T. P. Comyn, O. Cespedes, G. Chastanet, M. A. Halcrow, *Inorg. Chem.* **2015**, *54*, 6319–6330.

[12] a) I. C. Berdiell, R. Kulmaczewski, N. Shahid, O. Cespedes, M. A. Halcrow, *Chem. Commun.* **2021**, *57*, 6566–6569; b) K. S. Kumar, B. Heinrich, S. Vela, E. Moreno-Pineda, C. Bailly, M. Ruben, *Dalton Trans.* **2019**, *48*, 3825–3830.

[13] V. Garcia-Lopez, M. Palacios-Corella, A. Abherve, I. Pellicer-Carreno, C. Desplanches, M. Clemente-Leon, E. Coronado, *Dalton Trans.* **2018**, *47*, 16958–16968.

[14] M. B. Bushuev, V. P. Krivopalov, E. B. Nikolaenkova, K. A. Vinogradova, Y. V. Gatilov, *Dalton Trans.* **2018**, *47*, 9585–9591.

[15] Z. G. Lada, K. S. Andrikopoulos, C. D. Polyzou, V. Tangoulis, G. A. Voyiatzis, *J. Raman Spectrosc.* **2020**, *51*, 2171–2181.

[16] M. Cavallini, I. Bergenti, S. Milita, J. C. Kengne, D. Gentili, G. Ruani, I. Salitros, V. Meded, M. Ruben, *Langmuir* **2011**, *27*, 4076–4081.

[17] a) E. J. Devid, P. N. Martinho, M. V. Kamalakar, I. Salitros, U. Prendergast, J. F. Dayen, V. Meded, T. Lemma, R. Gonzalez-Prieto, F. Evers, T. E. Keyes, M. Ruben, B. Doudin, S. J. van der Molen, *ACS Nano* **2015**, *9*, 4496–4507; b) A. Abherve, M. J. Recio-Carretero, M. Lopez-Jorda, J. M. Clemente-Juan, J. Canet-Ferrer, A. Cantarero, M. Clemente-Leon, E. Coronado, *Inorg. Chem.* **2016**, *55*, 9361–9367; c) M. Attwood, H. Akutsu, L. Martin, T. J. Blundell, P. Le Maguere, S. S. Turner, *Dalton Trans.* **2021**, *50*, 11843–11851.

[18] Y. Miyazaki, T. Nakamoto, S. Ikeuchi, K. Saito, A. Inaba, M. Sorai, T. Tojo, T. Atake, G. S. Matouzenko, S. Zein, S. A. Borshch, *J. Phys. Chem. B* **2007**, *111*, 12508–12517.

[19] A. Abherve, M. Clemente-Leon, E. Coronado, C. J. Gomez-Garcia, M. Lopez-Jorda, *Dalton Trans.* **2014**, *43*, 12804–12804.

[20] a) M. A. Halcrow, *Chem. Soc. Rev.* **2011**, *40*, 4119–4142; b) Y. Hasegawa, R. Sakamoto, K. Takahashi, H. Nishihara, *Inorg. Chem.* **2013**, *52*, 1658–1665.

Chemistry–A European Journal

Research Article
doi.org/10.1002/chem.202103853

Chemistry
Europe
European Chemical
Societies Publishing

[21] L. J. K. Cook, R. Kulmaczewski, O. Cespedes, M. A. Halcrow, *Chem. Eur. J.* **2016**, *22*, 1789–1799.

[22] L. J. K. Cook, H. J. Shepherd, T. P. Comyn, C. Balde, O. Cespedes, G. Chastanet, M. A. Halcrow, *Chem. Eur. J.* **2015**, *21*, 4805–4816.

[23] M. Haryono, F. W. Heinemann, K. Petukhov, K. Gieb, P. Muller, A. Grohmann, *Eur. J. Inorg. Chem.* **2009**, *2009*, 2136–2143.

[24] I. Salitros, O. Fuhr, A. Eichhofer, R. Kruk, J. Pavlik, L. Dlhan, R. Boca, M. Ruben, *Dalton Trans.* **2012**, *41*, 5163–5171.

[25] J. J. Whittaker, P. Harding, J. K. Clegg, D. J. Harding, *Cryst. Growth Des.* **2020**, *20*, 7006–7011.

[26] a) L. J. Kershaw Cook, R. Kulmaczewski, S. A. Barrett, M. A. Halcrow, *Inorg. Chem. Front.* **2015**, *2*, 662–670; b) N. Mochida, A. Kimura, T. Ishida, *Magnetochemistry* **2015**, *1*, 17–27.

[27] J. A. Real, A. B. Gaspar, V. Niel, M. C. Muñoz, *Coord. Chem. Rev.* **2003**, *236*, 121–141.

[28] N. Bridonneau, L. Rigamonti, G. Poneti, D. Pinkowicz, A. Forni, A. Cornia, *Dalton Trans.* **2017**, *46*, 4075–4085.

[29] I. Galadzhun, R. Kulmaczewski, O. Cespedes, M. Yamada, N. Yoshinari, T. Konno, M. A. Halcrow, *Inorg. Chem.* **2018**, *57*, 13761–13771.

[30] R. Kulmaczewski, E. Trzop, L. J. Kershaw Cook, E. Collet, G. Chastanet, M. A. Halcrow, *Chem. Commun.* **2017**, *53*, 13268–13271.

[31] R. Kulmaczewski, E. Trzop, E. Collet, S. Vela, M. A. Halcrow, *J. Mater. Chem. C* **2020**, *8*, 8420–8429.

[32] *CrysAlisPRO*, Oxford Diffraction/Agilent Technologies UK Ltd., Yarnton.

[33] G. M. Sheldrick, *Acta Crystallogr. Sect. A Found. Adv.* **2015**, *71*, 3–8.

[34] G. M. Sheldrick, *Acta Crystallogr. Sect. C Struct. Chem.* **2015**, *71*, 3–8.

[35] O. V. Dolomanov, L. J. Bourhis, R. J. Gildea, J. A. K. Howard, H. Puschmann, *J. Appl. Crystallogr.* **2009**, *42*, 339–341.

[36] R. Ketkaew, Y. Tantirungrotechai, P. Harding, G. Chastanet, P. Guionneau, M. Marchivie, D. J. Harding, *Dalton Trans.* **2021**, *50*, 1086–1096.